Traveling surface undulation on a Ni-Mn-Ga single crystal element

Andrew Armstrong[1], Bibek Karki[1], Aaron Smith[2], Peter Müllner[1]

[1]Micron School of Materials Science and Engineering, Boise State University, Boise, ID, 83725, USA

[2]Shaw Mountain Technology LLC, Nampa, ID, 83687, USA

*corresponding author email: petermullner@boisestate.edu

Abstract

Active materials couple a stimulus (electrical, magnetic, thermal) with a mechanical response. Typical materials such as piezoelectrics strain as bulk materials to the stimuli. Here we consider an undulation created by *heterogeneous* deformation within a magnetic shape memory alloy (MSM) transducer. We study the mechanical response of an MSM element vs. two surface treatments: a *polished* state with minimal surface stresses, and a *micropeened* state with compressive surface stress. The polished element had a sharp-featured, faceted trough shape. The micropeened element had a smooth trough shape and an additional crest. The undulation was created by a rotating localized magnetic field, which caused heterogeneous variation of the twin-microstructure. For the polished and micropeened elements, the twin-microstructures were coarse and fine, respectively. For the polished element, the undulation moved by the nucleation of a few twin boundaries, which traveled along the entire element. For the micropeened sample, the twin boundaries moved back and forth over a short distance, thereby creating a dense twin lamellar, which formed the trough. The motion of the lamellar approximated the single thick twin while allowing additional degrees of freedom due to increased mobile interface density and different initial conditions of domain volume fraction. The dense twin microstructure also smoothed the magnetic flux pattern. The undulation amplitude was about 40 μm for the sample in both treatments.

Keywords: magnetic shape memory alloy; surface treatment; shotpeening; laser profilometry; MSM pump, Ni-Mn-Ga, inhomogeneous magnetic field.

1. Introduction

Classically, active materials strain uniformly to the stimuli. Piezoelectric elements, for example, actuate by electrical impulses which uniformly strain the transducer in, for example, new mixed perovskite materials with reversible strains of up to 0.6% [1]. The coordination of many transducer elements enables large strokes as well as complex and precise motion such as that found for ultrasonic traveling wave motors and piezowalk actuators [2]. Here we evaluate a magnetic shape memory alloy (MSM) transducer, which strains heterogeneously within. A locally strained region causes a trough on the transducer surface. The trough moves along the transducer surface with the rotation of a magnetic field [3]. While propagating, the trough is in an equilibrium state created by the magnetic field. When the rotation of the magnetic field is halted, the trough stops moving and remains in place.

Reversible plastic deformation of MSM alloys by magnetic field was discovered around 1996 [4-6]. MSM materials act as metallic muscles capable of longitudinal strain [7, 8], bending [9-11], and localized constriction [12] in magnetic fields. In MSM alloys, crystallographic twinning accommodates the deformation [13]. For the most commonly used Ni-Mn-Ga compositions, which have a 10M crystal structure, the maximum magnetic-field-induced strain is 7% [14]. High magneto-crystalline anisotropy [15], combined with highly mobile twin boundaries [16, 17], enables the magnetic-field-driven motion of twin boundaries and presents the two conditions necessary for magnetic-field-induced strain (MFIS).

An optimal MSM element has a strain close to the theoretical limit in addition to long fatigue life. Elements that have demonstrated good fatigue life have a dense twin microstructure [18]. Here the twin boundaries are mobile but move only short distances, retarded by interacting twins and surface constraints. Modification to the sample's surface by surface damage [19, 20], roughness [21], and coatings [22, 23] can constrain the sample surface and lead to a fine twin microstructure . Rigid edge constraints also affect the mechanical response.

MSM elements treated via our recently reported surface hardening technique, micropeening, are capable of 5% MFIS while also having a fatigue life greater than 10^6 cycles as a result of the dense twin microstructure [18, 24]. The residual compressive stress created by micropeening hinders crack nucleation on the surface, and the treatment smooths the mechanical response of the element. Rather than deforming sharply as a twinning plateau, the strain increases smoothly with magnetostress. The effects of a similar tailor-made fine twin structure on a sample have been studied for push-pull actuators actuated with a uniform magnetic field [24].

Here we consider the effect of micropeening upon an element locally actuated in a heterogeneous magnetic field in the manner of an MSM micropump [25-27]. The rotation of a magnetic field underneath an MSM element causes a local deformation to move across the element's top surface as it follows the magnetic field. An MSM micropump uses this translating cavity to pump small amounts of fluid up to a maximum pressure of 10 bar [26]. The stress state within the element is a combination of magnetostress, external stress, and surface constraints [28]. Surface constraints can be created by surface treatments and external forces, including fixturing and the Maxwell force which attracts the ferromagnetic element to the magnet. The actuation mechanism of the MSM element is thus complex [29, 30].

In this study, we measured the mechanical response of an MSM element with stress-free, polished surfaces. We then micropeened the same element's surfaces to induce a dense twin microstructure and studied the mechanical response of the MSM element. The experiment allowed us to compare the mechanical response of the transducer for the two surface treatments to the corresponding magnetic simulations. With this data, we propose a model to describe the microstructural changes which lead to the observed mechanical response.

2. Experimental

2.1 MSM element preparation

A $Ni_{50}Mn_{28.5}Ga_{21.5}$ single crystal grown in a modified Bridgeman furnace, according to Kellis *et al.*, was used in this study [17]. The structure was 10M martensite[31, 32], which is typical for MSM actuators. The martensite to austenite transition temperature (*i.e.*, the upper thermal limit for MSM functionality) was 315K. We cut the element from the boule along {100} and ground it to a parallelism of 10 μm with a Struers Accustop. We polished sequentially to a final polish using a 0.3 μm aluminum oxide slurry. The prepared element was 2.0 mm wide x 1.4 mm thick x 20 mm long.

The element was mounted onto a 0.25 mm thick glass coverslip with 0.1 mm thick double-sided 3M scotch tape. The tape allowed for localized strain while holding the sample in place. We transferred the MSM element from one test to another on the slide to avoid modifying the twin microstructure by handling the element. We initially trained the element on the slide by turning it 20 times between a parallel and perpendicular orientation within a homogeneous 1.5 T magnetic field and removed the element from the electromagnet with the magnetic field parallel to the sample's long axis. This training established a single domain structure where the *c*-axis was oriented parallel to the long axis of the element.

2.2 Laser measurement stage

Figure 1 is a diagram of the custom non-contact laser measurement stage. A stepper motor rotated a diametrically magnetized cylindrical N52 magnet behind the MSM element. The element surface was measured with a laser (Keyence LK-HO52) which was fixed to an optical table. The motor, magnet, and MSM element were translated orthogonal to the laser beam by a motorized linear stage (Thorlabs PT1-Z8). Fig. 1b shows a magnified view of the system sliced orthogonal to the stage. The MSM element mount was attached to the stage and clamped by a polycarbonate top plate. The plate had a 0.5 mm wide slot to allow the laser beam to reach the element surface. The pressure bearing beams of the top plate were only 0.5 mm thick. Thus, while constraining, the pressure beams flexed slightly under the clamping load. The top plate was compressed onto the element using nylon screws (not shown). In Fig. 1b, at $\alpha = 0°$, the magnetic north was parallel to the MSM element and pointed to the left. Rotating the permanent magnet clockwise (CW) from $\alpha = 0°$ caused the magnet's north pole to turn towards the MSM element.

When conducting a test, the user ran the motorized linear stage across the stationary Hall sensor and/or laser beam. For the following description, we consider a coordinate system fixed on the sample stage. When the stage traveled along negative x, the laser scanned the sample in the positive x direction. We performed three different test types, as shown in the schematics of Fig. 1c, 1d, 1e. The angle α describes the rotation of the magnet and the direction of the magnetic field. In the first test (Fig. 1c), we recorded the Hall sensor's output, which was placed 0.5 mm above the traveling stage. We simultaneously rotated the magnet at 2.5 Hz and moved the stage (with the magnet) under the Hall probe at 0.5 mm/s. The laser's sampling rate was 1000 Hz.

For the second test (Fig. 1d), we placed the MSM element/glass slip onto the stage centered on the magnet. Then, using the laser and beginning at $\alpha = 0°$, we scanned the top surface of the MSM element while leaving the magnet stationary. This gave the surface profile of the MSM element. We then set the magnet by the stepper motor to $\alpha = 18°$, and repeated the experiment. We continued with this procedure in 18° increments for α up to $\alpha = 720°$. We then repeated the procedure in reverse order, i.e., stepping the angle backward from $\alpha = 720°$ to $\alpha = 0°$.

For the third test (Fig. 1e), we kept the laser and the stage stationary. We measured the MSM element surface elevation as the magnet spun at 2.5 Hz underneath. The sample and the laser were centered on the position where the magnet is closest to the MSM element.

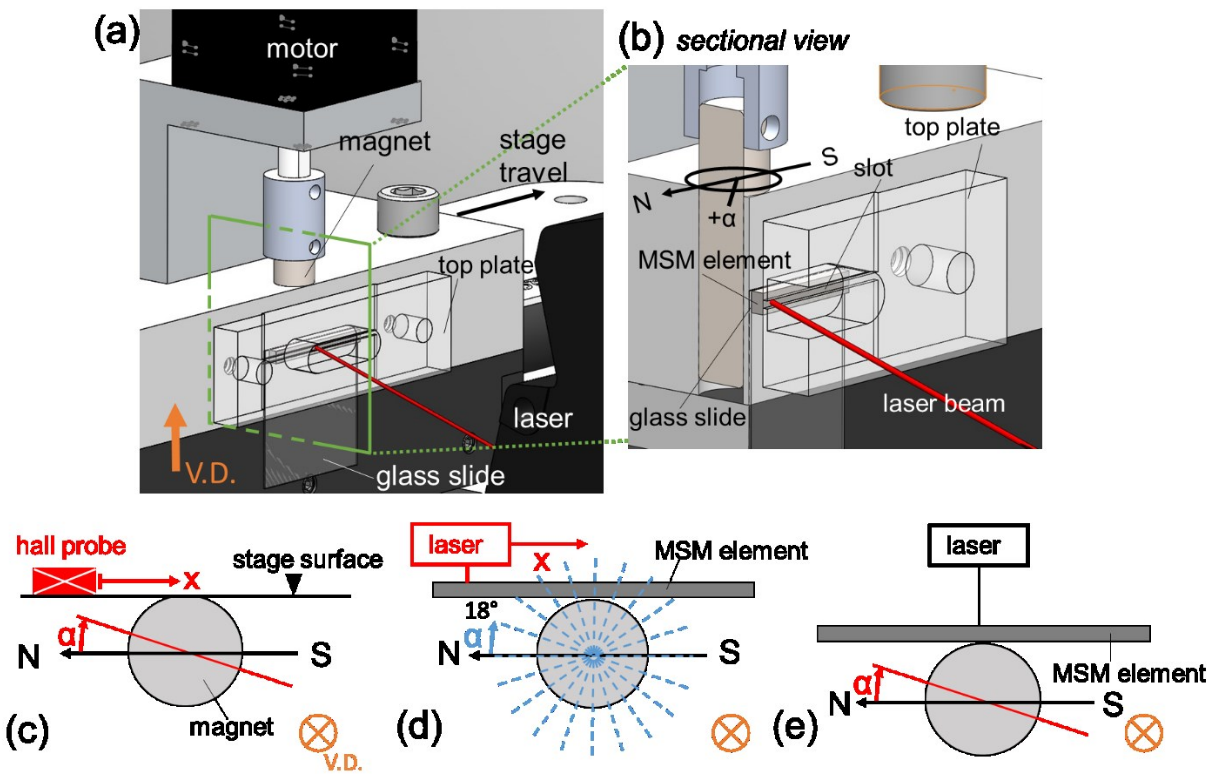

Fig. 1: Physical and schematic drawings of tests using the laser measurement system. (a) A stepper motor rotated a diametrically magnetized cylindrical magnet behind the MSM element. The laser measured the element surface elevation. A linear motor moved the stage. (b) shows the sectional view of the green box in (a). The MSM element was taped to a thin glass slide, which was mounted onto the stage. We held the MSM element down with a polycarbonate top plate, which had a window for the laser beam. The view direction (VD) is indicated in orange. The coordinate system centered upon the magnet is shown in (b). Figures (c), (d), and (e) are schematics of the tests. Components in red were active during each test, *i.e.*, translation and rotation. (For simplicity, we show here the scanning direction of the Hall probe and laser, in reality, the stage moves but in the opposite direction.) Components in blue were active between tests, *i.e.,* we scanned the element surface after rotation of the magnet an increment to magnetic field angle α. In (c), the Hall probe scanned the magnetic field along the stage. In (d), the magnet rotated in 18° increments, and a laser measured the surface profile at each increment. In (e), the magnet rotated at 2.5 Hz, and the laser was positioned in the center and held stationary to measure the element surface undulation.

2.3 Optical microscopy test block

We built an apparatus to view the twin microstructure under a Leica DM6000 optical microscope (Fig. 2a). An N52 permanent magnet was turned by a gearhead micromotor equipped with an optical encoder (Namiki SBL07). We placed the element on the block and fixed the glass slide from the top with mounting putty. Using the coordinates and convention for the rotation defined for the laser experiments (Fig. 1d), we positioned the magnet at 18° intervals (Fig. 2b). We imaged the active region (ROI), boxed in red in Fig. 2b, using the microscope's default image stitching software. We imaged 20 magnetic field positions (*i.e.*, a full revolution of the magnet). Local contrast was enhanced using the CLAHE process of the FIJI image processor to improve the contrast between twins.

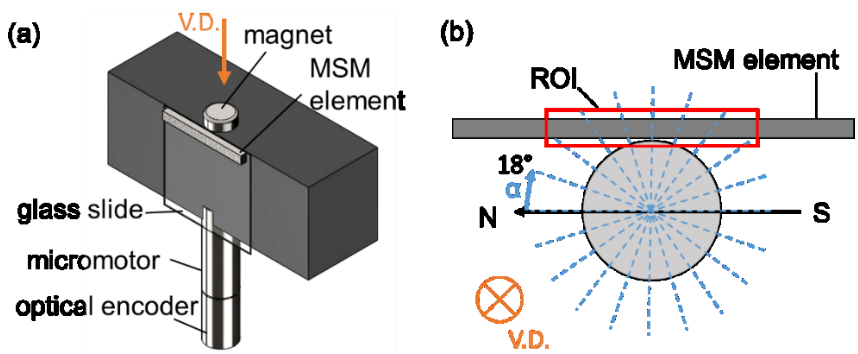

Fig. 2: Drawing and diagram of the microscopy block. (a) The micromotor rotated the magnet to angle α, and a micrograph of the twin microstructure of the element side was taken along direction VD. (b) The magnet rotated in increments of 18° between micrographs. The red box marks the region of interest (ROI) of the MSM element which actuated.

2.4 Micropeening

After recording laser measurements and optical tests on the polished element, we removed the element from the supporting glass slide. We then removed the tape residue with acetone. The element was micropeened according to the procedure discussed in Zhang *et al.* [18]. In brief: the element was heated to 80° C, thereby transforming to austenite. The element was micropeened for 8 sec at 1.75 bar with 50 μm glass beads. The element was micropeened on its top and bottom surfaces with respect to the viewing direction shown in Figure 2. When cooled back to martensite, the MSM element was again taped to the glass slide. The twin microstructure following from the phase transformation was oriented using an electromagnet. After conducting the laser and optical tests on the micropeened element, we cast the element in cyanoacrylate, then polished the top surface to reveal the twin microstructure with 0.3 μm alumina slurry. During this polishing process, we removed about 5 μm of material.

3. Computer Simulation

We used a 2D magnetostatic finite element analysis software (FEMM) to simulate the interaction of the twin microstructure and the magnetic field. In our model, the 10M martensite MSM element contains two orthogonal crystallographic directions whose lattice parameters are *a* and *c*. The *c*-axis is the short direction (i.e., the material shrinks along the *c*-axis), and also the axis of easy magnetization. We use relative permeability values of (2, 40) along the (*a, c*) axis to model the magnetic anisotropy of these two twin domains in the crystal [33]. FEMM allows simulating either anisotropic material properties using linear approximation, or a B-H curve, but not both simultaneously. We used the linear anisotropy approximation, which extends the magnetization past the material's saturation magnetization. Thus, the simulations overestimate the flux density and magnetic anisotropy. We did not model the material's dimensional change, as it was small compared to the bulk dimension.

The simulated element was the same size as that of the element used in experiments. We label the parent twin domain H_{twin} since it has the *c*-axis along horizontal, *i.e.*, it is contracted horizontally and expanded vertically. The other twin domain, labeled V_{twin}, has the *c*-axis along vertical, *i.e.*, it is expanded horizontally and contracted vertically. The gap between the magnet and the MSM element was 0.5 mm. A band of twin domain, V_{twin}, was inserted within the parent domain, H_{twin}, as approximated from the micrographs. For the polished sample, we modeled a thick V_{twin} thickness of 1.4 mm with twin centroid at 1.4 mm left (α = 54°) and right (α = 126°) of the center of the MSM element.

The micropeened sample was simulated as a lamellar (*i.e.*, a stack of plates) of 25 μm lamella. With three of four lamella having *c* in the horizontal direction, the stack has *c* predominately in the horizontal direction, or $H_{lamellar}$, in which case the material expands vertically and contracts horizontally. With one of four lamella having *c* in the vertical direction, or $V_{lamellar}$, the material shrinks vertically and expands horizontally.

The simulated twin bilayer was 100 μm, or about five times thicker than measured experimentally for the micropeened twin structure. We chose this density because of the limited computing power available in this study.

4. Results

4.1 Measurement of the magnetic field

Fig. 3 gives the vertical component of the magnetic field along the stage. At 10 mm to the left or right from the center of the stage surface, the magnetic field was about 50 mT. At the center of the stage on the surface, the field was nearly 600 mT. The blue dashed lines drawn at ±200 mT indicate the estimated region of sufficient magnetic field to move boundaries of Type I twins. The measurement was only an estimate, as induced magnetization is a function of the twin microstructure and the horizontal component of the magnetic field, which biases the *c*-axis horizontally.

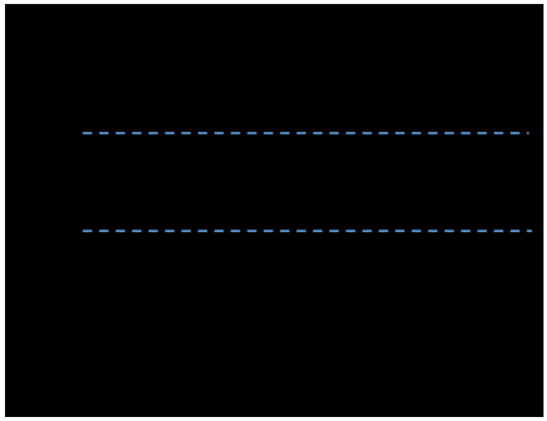

Fig. 3: Measurement of the magnetic field along the stage. The profile was obtained by rotating the magnet while advancing the stage. The blue dashed lines show the estimated switching field for actuation by the Type I twinning mechanism.

4.2 Laser measurements

Fig. 4 shows CW surface profiles for the polished (a) and micropeened (b) element measured by the laser. The bottom black profiles are the experimental data of the element measured without the magnetic field (we removed the magnet and longitudinally compressed the element.) The red profiles are experimental data of the surface profile taken at $\alpha = 90°$. To obtain the blue line, we subtracted the baseline from the $\alpha = 90°$ profile. Localized horizontal extension and contraction prevented full alignment with the baseline profile, resulting in some noise. Sharp peaks were artifacts caused by slight laser instability at coarse twin interfaces. The existence of these artifact made comparisons challenging with profiles superimposed. We thus filtered out high frequency elements for superimposed profile analysis using Butterworth filter in MATLAB 2019a (green top profile), a cutoff wavenumber of 0.5 mm^{-1} and an order parameter of $n = 3$. The deformation of the polished element was approximately an asymmetrical, faceted, triangular trough. The micropeened element had a smoother, more symmetrical trough and formed an additional crest beside the trough. Comparing the baseline profiles, the micropeened element had greater curvature along the length of the element.

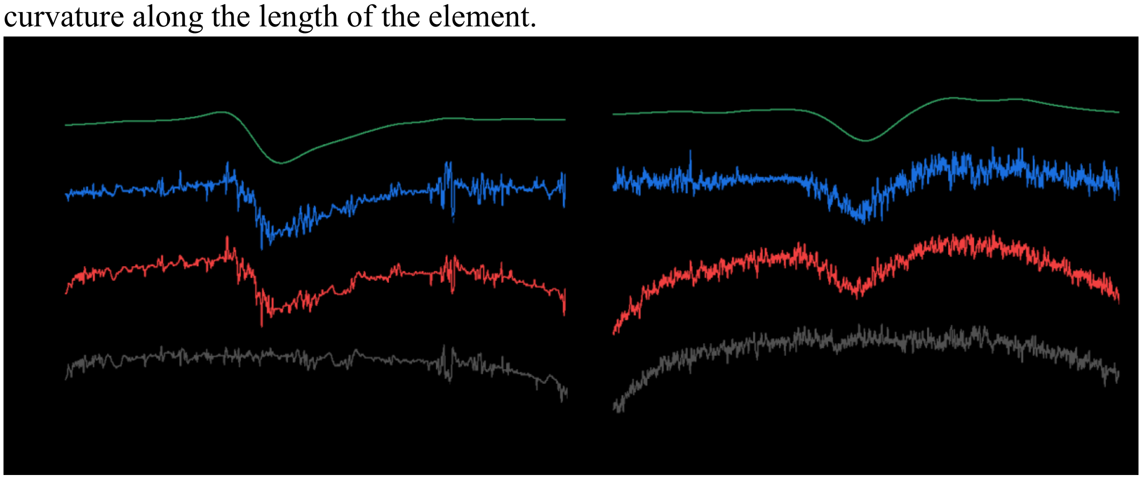

Fig. 4: Elevation profiles at locations along the MSM element for the two different surface treatments. The bottom profile (black) was the baseline scan of the element without a magnetic field. The red scan was taken at $\alpha = 90°$. The

blue scan is the difference between baseline and $\alpha = 90°$ scan. The blue scan was filtered in MATLAB 2019a with a Butterworth filter. The green scan is the filtered output (a) Polished element surface profile. (b) Micropeened element surface profile.

4.2.1 Surface profiles

The profiles taken at the different magnet angles were plotted together in Fig. 5. Figure 5a shows the baseline-removed raw data during CW actuation of polished element. The figure reads from bottom to top. The high frequency element to the surface profiles are an artifact of the instability of the laser beam across sharp interfaces between twin variants, which cause associated change in reflection and is thus not necessarily capturing the true surface height. Macroscopically, a similar effect is seen when encountering sharp transitions (such as when scanning onto the MSM element from the stage.) Additionally, for comparison of superimposed profiles, (such as Fig. 5b) the high-frequency noise drowns out the subtler comparisons between angular positions.

Fig. 5b shows the filtered and superimposed data for the polished element actuated CW. At $\alpha = 0°$, the element had a nearly symmetrical trough centered at $x = 2.7$ mm. At $\alpha = 18°$, troughs were present at $x = \pm2.7$ mm. The trough at 2.7 mm reduced in size while the new trough formed at -2.7 mm. The newly formed trough deepened and moved to the right as the magnet rotated CW. The left slope of the newly-formed trough (arrow 1) was steep and nearly constant from $\alpha = 54°$ to $\alpha = 90°$. At $\alpha = 90°$, the element rose slightly (arrow 2) behind the trailing edge of the trough. On the right side, the trough slope had a distinct disinclination (arrow 3). For the profiles from $\alpha = 36°$ to $\alpha = 90°$, the right shoulder of the trough (arrow 4) did not move and appeared to be pinned at 2.2 mm. The profile became nearly symmetrical with further rotation. See Supp. Fig. 1 for the full range of scans of the polished sample.

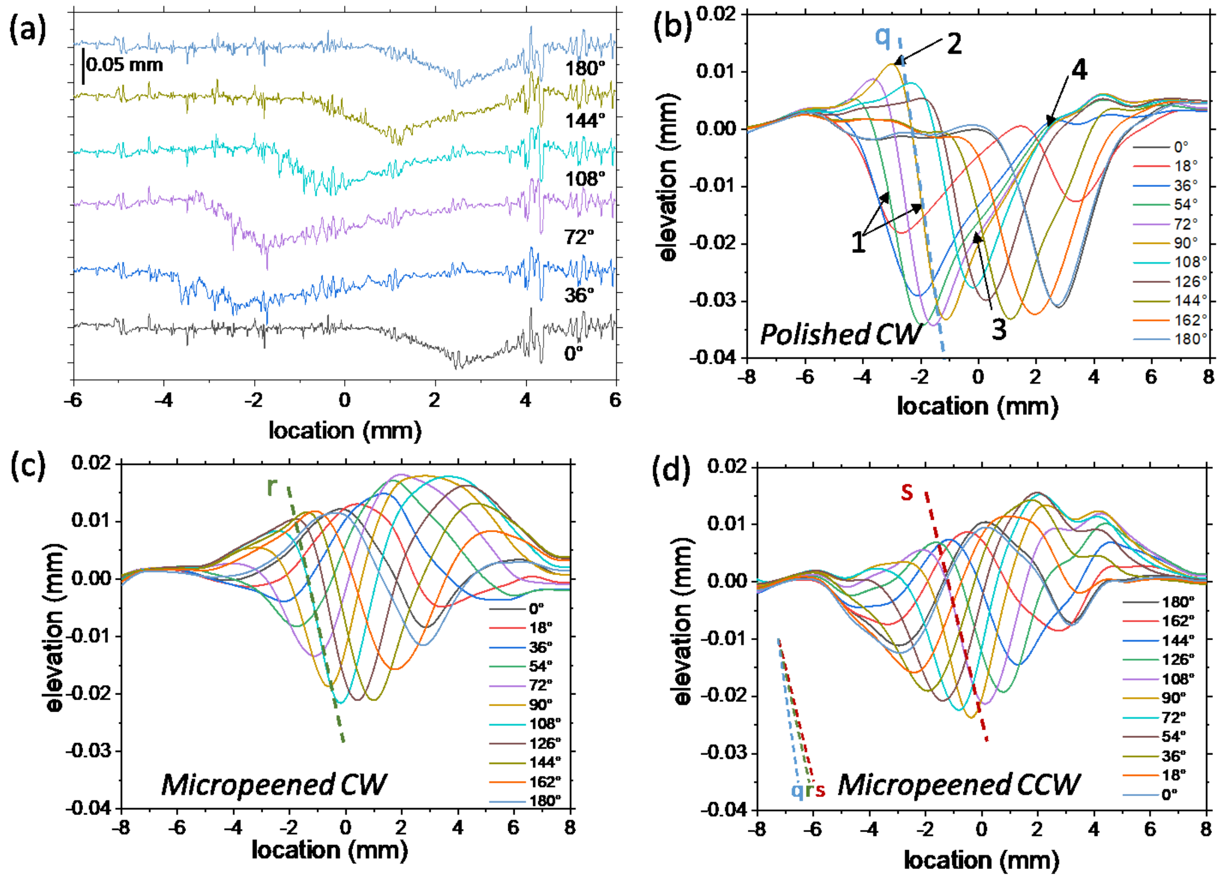

Fig. 5: MSM element surface profiles during half revolution of the magnet. (a) Baseline-corrected, non-filtered profiles as the magnet swept CW under the polished element. The sharp spikes in the profiles occurs at sharp variant boundaries, which cause slight laser instability, and combined with high sampling rate led to high frequency artifacts at variant interfaces. (b) The MATLAB filtered profiles of the polished sample as the magnet rotated CW. The arrowed numbers point to behaviors discussed further in the text. (c) The filtered profile of the micropeened sample as the magnet rotated CW. (d) The filtered profile of the micropeened sample as the magnet rotated CCW. The dashed lines indicate the slope of the left side of the trough. The slopes are reproduced in the bottom left of (d). q has a comparatively greater slope than r or s.

Figure 5 shows the surface profile of the micropeened sample with the field rotated CW (Fig. 5c) and CCW (Fig. 5d). In Fig. 5c, at $\alpha = 0°$, the trough centers were at 3 mm and -4 mm. With the CW rotation of the magnet, the right trough deepened, and a crest grew correspondingly. At $\alpha = 90°$, the top of the crest was 18 μm above the baseline, and the trough was 18 μm deep. While the crest was asymmetrical about $x = 0$, being much larger on the right, the depth of the trough was more symmetrical about $x = 0$. In Fig. 5d, the magnet rotated CCW. The strain amplitude was slightly greater for the CW actuation, while the width of the strain envelope was nearly the same for both treatments and directions, from -5 mm to 7 mm. The dashed lines in Fig. 5b, 5c, 5d highlight the steepest left slop for each case, which was steepest for the polished sample (q), less steep for the micropeened sample actuated by CW magnetic field rotation (r), and least steep for the micropeened sample actuated by CCW magnetic field rotation (s), as shown comparatively in the lower left corner of Fig. 5d. See Supplemental Fig. 2 for the full range of scans of the micropeened sample.

The north and south poles actuate identically, as seen by the similarity of $\alpha = 0°$ and 180° profiles in 5c and 5d. However, in Fig. 5c, there is a noticeable difference in the trough depth, nearly 5 μm, between 0° and 180°. The result could be due to a slight training effect or some source of hysteresis in the system. The position of the maximum crest was on the right irrespective of rotation direction.

4.2.2 Elevation variation in the center of the MSM element

Figure 6 shows surface elevation measured at the center of the element as the magnet rotated underneath at 2.5 Hz. We captured a snapshot of the twin boundary movement in time. The polished sample transformed quickly when elevating (1) and slowly when depressing (2). The crests (3) and troughs (4) transition at roughly the same rate, which is evident by the equidistant crest and trough widths. The micropeened element had a broader crest and narrower trough when actuated CW, which indicates a propensity for the element to remain elevated in the top position, in a crest. When rotated CCW, the transition rate was slow in the trough and fast in the crest. Black arrows (5) point to slight shoulders on the downward transition, found for both surface treatments. The position and width of the shoulder are located at slightly different locations of the transition for various surface treatments and actuation directions.

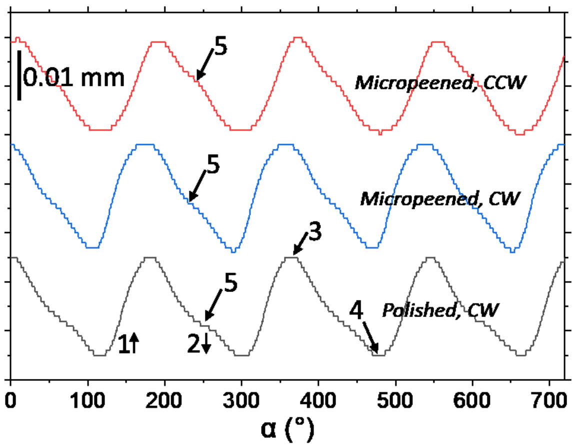

Fig. 6: Laser measurement at the center of the element as the magnetic field rotated. In black, the polished sample as the magnetic field rotated CW. In blue, the micropeened sample as the magnet rotated CW. In red, the micropeened sample as the magnet rotated CCW. The arrow on each curve points to a transition further discussed in the text. The fine steps are due to the resolution of the laser.

4.3 Microscopy

Figure 7a shows a side profile of the twin microstructure for the polished sample taken at α = 54°. The polished sample had a thick V_{twin} domain. The dashed lines mark the twin boundaries. A few thin V_{twin} domains nucleated on the right side (*i.e.*, ahead) of the thick V_{twin} domain. Figure 7b is a micrograph of the micropeened element, captured at α = 90°, which shows a dense twin microstructure. While the element had actuated, the mechanism of actuation was unclear as it was masked within the dense twin microstructure. Figures 7c and 7d show a top view of the polished (c) and the micropeened (d) elements at α = 0° with coarse and dense twin microstructures, respectively. The top surface of the polished sample has a few very thin and several intermediate twins. The width of the twin bilayer (*i.e.*, containing both V_{twin} and H_{twin}) varies, and one particular case is indicated by the white bar. The width of the bilayers varied from about 10 to 150 μm at this angle. For the micropeened element, the twin bilayer width was 10 μm, measured after polishing the surface to view the twins.

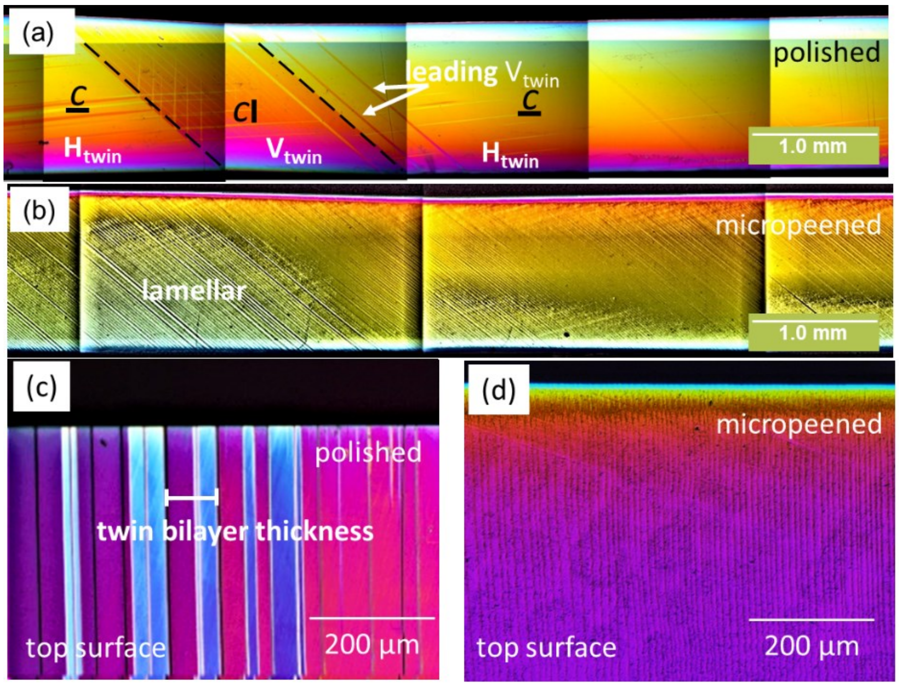

Fig. 7: Micrographs taken of the twin microstructure for the sample when polished (a, c) and micropeened (b, d). (a) At α = 54°, the sample has a thick V_{twin} in the parent H_{twin}, as viewed from the side. Thinner V_{twin} leads the motion of the thick V_{twin}. (b) At α = 90°, the twin microstructure of the micropeened sample, viewed from the side. The deformation is accommodated in the lamellar and not viewable at this magnification. (c) Viewed from the top, the twin structure for the polished sample. Domains show up as contrast across twin boundaries. The purple/red tones are the parent H_{twin}, and the blue the V_{twin} domain. The twin bilayer is the distance of the two twin domains, shown for the polished sample. (d) The lamellar microstructure as viewed from the top.

Figure 8 shows a sequence of micrographs for the side views of the (a) polished and (b) micropeened elements. To visualize the trough more clearly, we scaled the micrographs vertically by 10x. We highlighted the position of the twin boundaries, which appear much steeper than 45° due to 10x scaling. At α = 18°, the polished element was nearly a single domain H_{twin}. At 54°, an approximately 1.0 mm thick V_{twin} domain had nucleated and grown. This thick V_{twin} domain created an inclined facet on the top surface, which formed the left slope of the trough. The right slope of the trough had a few thin V_{twin} separating regions of the parent domain. At α = 90°, the V_{twin} domain had thickened to ~1.5 mm and moved to the right along the element. At 126°, the trough was composed of a few thick V_{twin} domains and numerous thinner V_{twin} domains. At 180°, the trough contained only thin V_{twin} domains and was more symmetrical. Further rotation of the magnetic field removed all V_{twin} domains. The motion repeated nearly identically when actuated by the south pole. We direct the reader to Suppl. Fig. 3 for the full sequence.

In Fig. 8b, the micropeened element has a smoother trough, which travels a greater distance along the element. At $\alpha = 18°$, a shallow trough is located at $x = -2$ mm, and a larger trough is located at $x = 4$ mm (truncated by the edge of the image). At $\alpha = 54°$, the left trough had deepened and moved to $x = -1$ mm, and the right trough had disappeared. The trough had moved further to $x = 0$, 1.3, and 2.3 mm for $\alpha = 90$, 126, and 180°, respectively. Supplemental Figs. 4 and 5 show snapshots of the moving surface undulation in the micropeened sample.

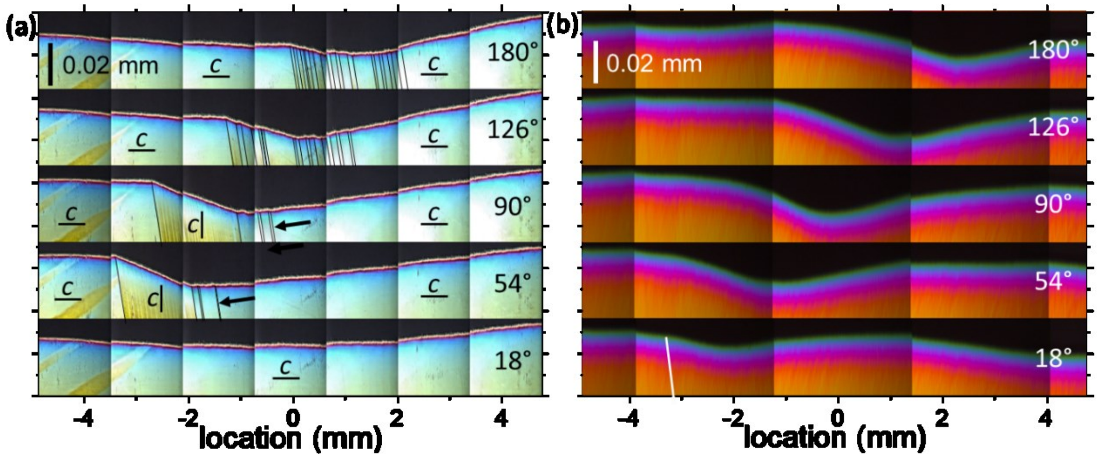

Fig. 8: (a) A sequence of micrographs taken for the polished sample as the magnetic field rotated CW. The micrographs were stretched 10x in the vertical direction, making the twin boundary appear much steeper than 45°. Reading from bottom to top: At 18°, the region is nearly a single domain of the parent H_{twin}. At 54°, a V_{twin} nucleated and thickened, creating the left slope of the trough. At 90°, the V_{twin} had the greatest thickness then broke apart as it moved along the element. At 136°, the thick V_{twin} broke apart into thinner V_{twin} and moved along the element. At 180°, the thick V_{twin} thinned further into multiple finer V_{twin} and moved along the element. The arrows point to leading V_{twin}, which creates the right slope of the trough. (b) The sequence for the micropeened sample. The twin boundaries of parent twin lamellar, $H_{lamellar}$, were oriented along the white line in the bottom micrograph.

To determine the motion mechanism of the trough for the fine twin microstructure, we plotted a contrast profile viewing the side, at the center of the element, as the trough moved past. Fig. 9 shows micrographs taken at $\alpha = 90°$, 108°, and 126°. In the contrast profile, the maximum thickness of the darker twin domain occurred at $\alpha = 90°$. Here, the width of the dark domain, which is V_{twin}, averaged 5 μm measured at full-width half max (FWHM). At $\alpha = 108°$, the V_{twin} domain decreased to a thickness of 3 μm FWHM and disappeared at $\alpha = 126°$. After rotating the magnet back and forth many times, we determined that the lamellar orientation did not change with rotation direction.

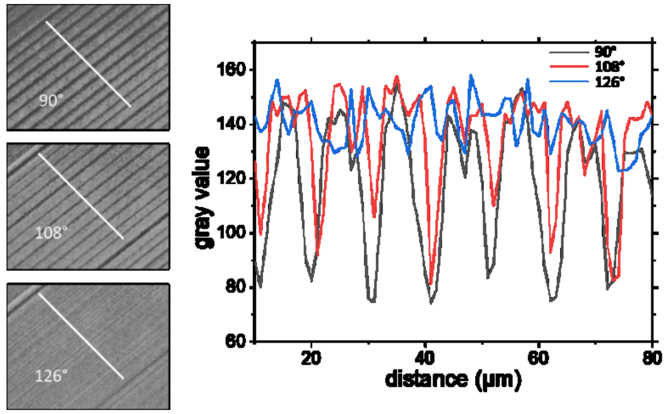

Fig. 9: For the micropeened sample, we used image analysis software to analyze the twin boundary motion, which caused the lamellar strain. The contrast of the twin domain was maximum at $\alpha = 90°$. With the rotation of the field, the dark twin domain gradually thins and disappears after 126°.

4.4 Simulation results

Figure 10 shows results of simulations of the magnetic field at $\alpha = 54°$ (a, b) and $\alpha = 126°$ (c, d) for the polished element (a, c) and the micropeened element (b, c). At $\alpha = 54°$ (Fig. 10a), the V_{twin} centroid was 1.4 mm left of the element center, and the magnetic field lines entered the twin vertically and were refracted across the right twin boundary. No flux lines exited across the left boundary of the V_{twin} or through the twin into the air above. The right half of the V_{twin} had a high flux density (800 mT), while the top left corner had a much lower flux density (100 mT). To check the sensitivity of the results on the twin boundary position, we moved the left twin boundary 1 mm further left in the model (not shown), resulting in a slight increase of the magnetic flux in the twin, however, without significantly changing the flux pattern. In Fig. 10c at $\alpha = 126°$, the V_{twin} centroid was 1.4 mm right of the element center. Here, less flux entered the twin, and the entering field diverged across both boundaries. To exit the left twin boundary, the field lines circled back to refract across the twin boundary into the parent H_{twin} domain.

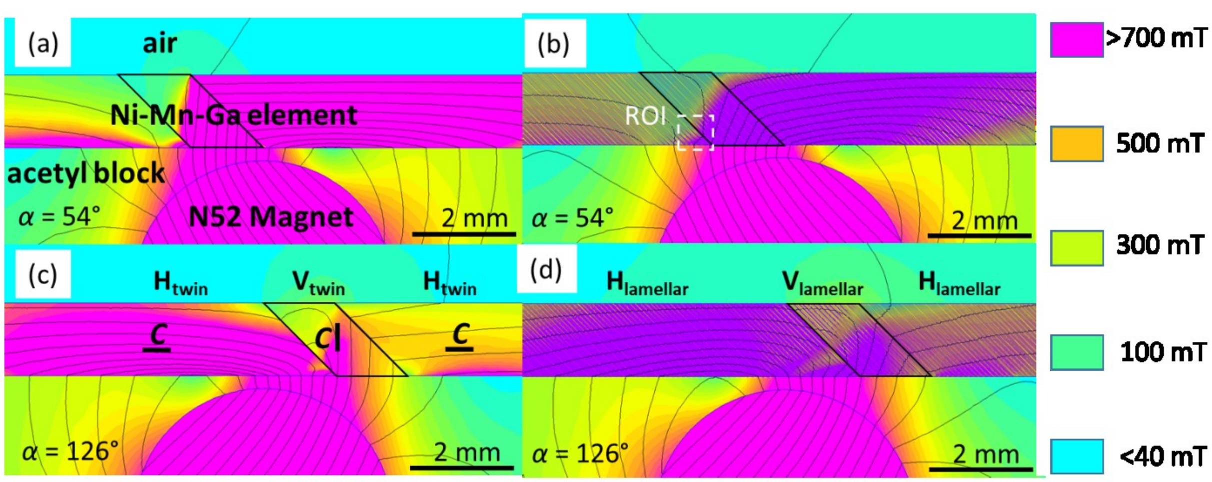

Fig. 10: FEMM simulations. The magnet is oriented at $\alpha = 54°$ in (a) and (b) and $\alpha = 126°$ in (c) and (d). Figures (a, c) and (b, d) show results for the polished and micropeened samples. We modeled a 1.4 mm thick twin domain (V_{twin}, a, c) and a 1.4 mm thick twin lamellar ($V_{lamellar}$, b, d) as described in Section 3. In (a), the field enters

vertically and is refracted across the right twin boundary. (b) For the micropeened sample, the field has a similar path but is smoother and more diffuse. The white dashed box (ROI) shows the region, which is enlarged in Fig. 11. In (c), at α = 126°, the twin is to the right of the center of the magnet. The twin only weakly magnetizes. In (d), the twinned lamellar had similar divergence but has slightly greater field intensity.

Figure 10b shows a simulation at α = 54° of the micropeened sample. In the parent $H_{lamellar}$, the microstructure is composed of thick H_{twin} and thin V_{twin} lamella. The twin $V_{lamellar}$ is composed of thick V_{twin} lamella and thin H_{twin} lamella. At interfaces between the twinned lamellar and parent lamellar, the field lines took sharper angles according to the change in volume fraction behind the interface, similar to the coarse twin boundary of Fig. 10a. Figure 11 shows a magnified view of the inset marked with a dashed box (ROI) in Fig. 10b, along with definitions of modeled $V_{lamellar}$ and $H_{lamellar}$. In the $H_{lamellar}$ domain, lamella with a vertical *c*-axis magnetized, but the flux tapered off up along the plate.

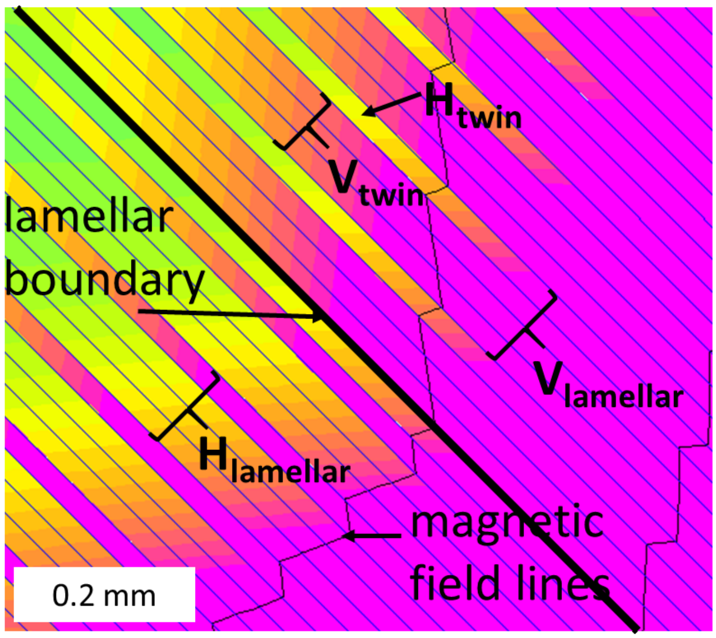

Fig. 11: Simulated flux schematic of the micropeened twin microstructure as defined by the ROI in Fig. 10. $H_{lamellar}$ was modeled as a repetition of three H_{twin} and one V_{twin}. $V_{lamellar}$ was modeled as a repetition of three V_{twin} and one H_{twin}. The magnetic field lines were deflected slightly by individual lamella and deflected significantly by lamellar boundaries. The lamellar boundary is not likely sharp as shown in the model, being related to the different volume fraction of domains, and the gradients which interconnect.

5. Discussion and conclusions

We discuss the mechanical response of the polished and micropeened MSM elements in the context of the laser measurements, micrographs, and existing literature. The constraints between the optical and the laser measurements differ slightly by the clamping mechanics. MSM alloys respond sensitively to constraints such as fixtures [34]. The constraints cause the differences in the geometry of the undulation when measured with the laser and the microscope. In the laser measurements, the element was clamped down, while for micrographs, it was unconstrained from the top. This difference was not expected to cause such a significant impact upon the mechanical behavior and so was not accounted for in the design of the study. We believe the constraint gives the two troughs seen on the polished profilometer measurements, but only one observed in the micrographs. The effect of the top constraint is substantial and should be considered when designing actuators.

In the literature, magnetic-field-induced deformation is often simplified as an axial strain. In reality, the local deformation state depends on the twin pattern. For a single twin boundary, the deformation is a shear. For a set of parallel twin boundaries, the deformation is a discontinuous shear. A set of wedged twins causes bending [9, 35]. These differences are significant in the formation of the trough. In particular, bending by wedged twins is required to form the "uphill" slope that counters the twinning shear, as shown in detail below.

5.1 Polished sample actuation

Figure 12 is a model of the twin-microstructure for the polished sample interpreted from Fig. 5b and 8a, which are the laser scans and micrographs of the element at discrete angles of α. The thick V_{twin} domain causes the constant slope down, as shown in Fig. 12 and Fig. 5b (arrow 1). The twin forms the facet. A slight crest at the trailing shoulder (shown by arrow 2 in Fig. 5b) occurs because the surface is forced away from the stage as the V_{twin} thickens, gently kinking up and away from the bottom. The transition (3) in Fig. 5b is created by thin leading wedged twins that turn the surface upward. These twins are visible in Fig. 8 and shown schematically in Fig. 12. The leading shoulder (arrow 4) is at a fixed position from $\alpha = 36°$ to $\alpha = 108°$. This shoulder is likely formed by a wedge twin of lower mobility, pinned by some obstacle.

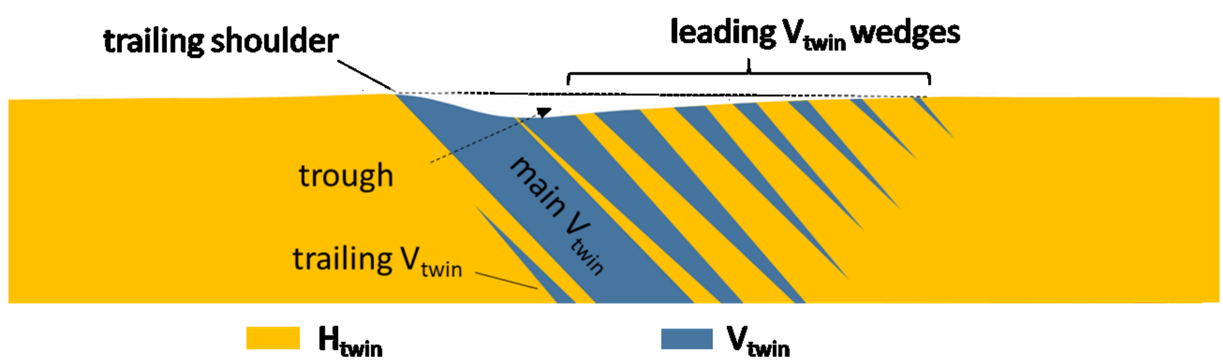

Fig. 12: Interpretation of twin structures found in the actuation of the polished sample. Wedge twins adjacent to the thick twin's left boundary formed to reduce interface surface stresses near the bottom. Leading wedged twins recover the height back to the parent twin. Wedge twins interface between the main V_{twin} and parent.

In the micrographs (Fig. 8a), we find a 100 μm thick V_{twin} domain at a location close to that of the shoulder, and also several wedge-like V_{twin}. The wedge angle is exaggerated in Fig. 12. The micrographs of the polished element showed no definitive shoulder, which is perhaps caused by the different constraints on the sample in the laser experiments.

5.2 Micropeened sample actuation

The micropeened sample has a twin microstructure much denser than that in the polished sample. Surface defects pin the twin boundaries [19, 23, 36] at the surface such that the twin boundaries cannot move over large distances. The cyclic magnetic field causes a periodic back and forth motion of the twin boundaries over a few microns. As a result, lamella expands and contracts with the field angle, similar to the motion of a bellow. Figure 9 shows how the twins gradually expand and contract. This expansion and contraction of fine twins have also been described by Straka *et al.* [11].

As the twin boundaries move back and forth, they slightly bend. This bending stems from the elastic interaction of twinning dislocations (disconnections) typical for materials with a high degree of defects, such as present in micropeened elements [37]. In Fig. 13, the smooth surface profile of the micropeened element is a result of subtle changes to each lamella. The twin lamella can expand and contract and create fine wedge twins that bend the element . The height of the surface depends upon the volume fraction of each twin domain. Reading from the far left, the volume fraction of V_{twin} and H_{twin} is equal, i.e., in between $H_{lamellar}$ and $V_{lamellar}$ the element having neither maximum nor minimum elevation with an intermediate strain. A crest is caused by parent (orange) volume fraction. Areas nearly completely twin lamellar (blue) are vertically compressed and form a trough. The troughs form when the ratio drifts in favor of the twin, and crest when it drifts in favor of the parent. Areas with blue wedges pointing down have a convex surface, those with orange wedges pointing down have a concave surface.

While the maximum curvatures occur near the center, much of the magnetic flux is carried through to the ends of the element, which directs magnetic flux back to the magnet (Fig. 10). When magnetic flux is parallel to the length of the element, the H_{twin} domain is preferred. Slight clamping force preferences the V_{twin} domain. The interplay between the clamping stress and magnetostress, therefore, locally affects the domain volume fraction within the lamellar. We expect the crests form due to the local stresses (mechanical and magnetic) within the element, which correlate to changes in local domain volume fraction in the lamellar. In the test, bulk longitudinal strain is prevented by the constrains, i.e. tape, friction, and clamping force. As one region of material shrinks, causing a trough, another corresponding part of material must expand to conserve the constrained volume. In the current scenario, pinned, fine TBs and external constraint implies volume conservation occurs through the formation of crests.

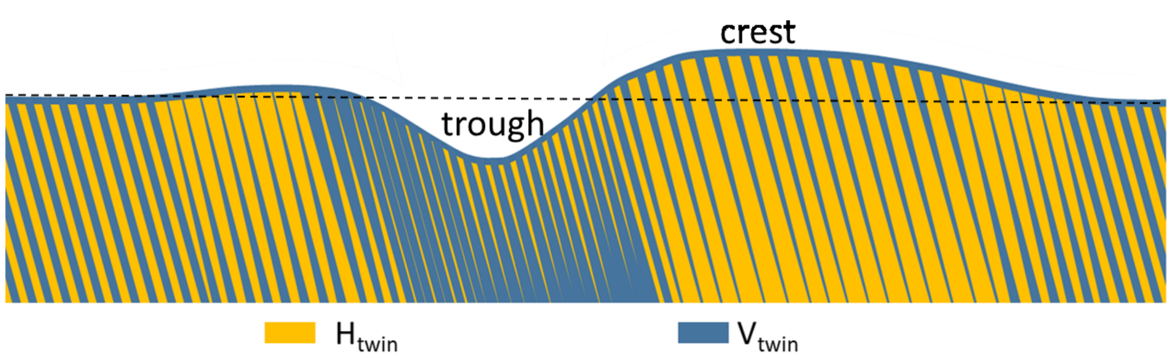

Fig. 13: Interpretation of twin structures found in the actuation of the micropeened sample. The surface profile is replotted from Fig. 5c at $\alpha = 90°$ and rescaled vertically. The surface elevation is dictated by the volume fraction of the two twins. H_{twin} - predominant lamellar (mostly orange) cause the surface to rise, as seen in areas of the crests above the vertically expanded H_{twin}. V_{twin} - predominant lamellar shrinks the material and forms a trough. Orange and blue wedges pointing down create concave and convex surfaces, respectively.

The damaged surface layer of the micropeened hardens the surface against strain. The magnetic field is sufficiently strong to move twin boundaries in the center of the element but not at the surface. The material strains against this surface and deforms the surface layer elastically. Upon polishing, we find something resembling a fine Type II twin structure [38] in the element center (shown in Supp. Fig. 6).

5.3 Model of trough motion in polished and micropeened samples.

Comparison of the micrographs, surface profiles, and the elevation variation at the center of the element due to magnet cycling yields a model of twin boundary motion of the polished and micropeened elements. In Fig. 14a, a V_{twin} nucleates then thickens by the motion of the right twin boundary. The wedge twins required for forming the trough (Fig. 12) are not shown in Fig. 14a for simplicity. The V_{twin} then migrates to the right by the simultaneous motion of both twin boundaries. Eventually, the leading (*i.e.*, right) twin boundary stops where the magnetic field is insufficient for activating its movement. The trailing twin boundary reaches the leading twin boundary and the two combine, which causes the V_{twin} to collapse and the trough to disappear. This mechanism was reported in 2012 [3].

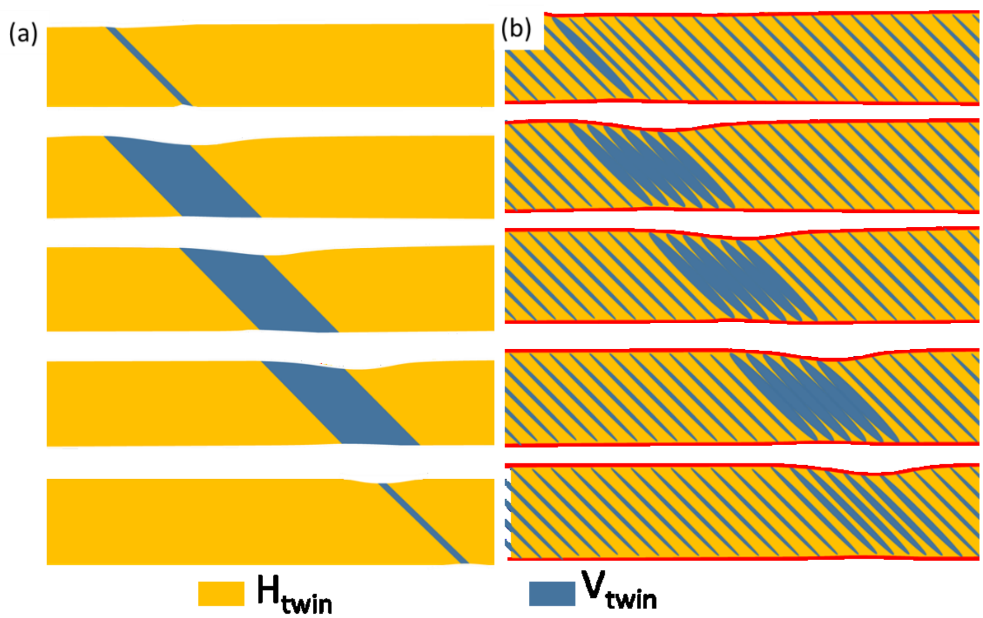

Fig. 14: Translational movement of the V_{twin} region through the H_{twin} and $H_{lamellar}$ for the different surface treatments. Red lines mark the stressed surface layer of the micropeened element. (a) The polished element has a single twin domain that nucleates and thickens, then moves along the element, then shrinks and collapses. (b) The micropeened $V_{lamellar}$, composed predominantly of V_{twin} plates, similarly nucleated, moved down the element, then dissipated into $H_{lamellar}$.

The micropeened MSM element has a finely twinned microstructure, as shown in Fig. 14b. When a magnetic pole points to a particular area, the blue twins in that area expand. Consequently, the fraction of blue twins is large in that area, and the twin region thickens to form the downward slope of the trough. When the magnetic pole moves away from that particular area, the twin boundaries retract, the blue twins become thin, and the MSM element widens. As the magnetic pole moves along the MSM element, the blue twins first thicken and then thin, and the area with thick blue twins propagates along the MSM element. The propagation of the package of thick twins resembles the motion of a wave packet, albeit it is a quasi-static motion, entirely controlled by the position of the magnetic pole.

Since the twins are pinned at the surface for the micropeened MSM element, some orange area remains present at any given time. Thus, the output strain is slightly less for the micropeened sample compared to the polished sample, which turns entirely blue during the downward slope of the trough. This reduced strain results in a slightly shallower trough for the micropeened MSM element, as shown with the dashed lines q, r, and s in Fig. 5d, which give maximum slopes for each case. The actuation is less because the magnetostress is insufficient to cause complete twinning and detwinning. Higher magnetostress would cause the lamellar to strain further and become more similar to the strain seen for the polished sample.

The transition marked as (5) in Fig. 6 is the transition between the thickening of the twin and the translational motion of the twin. We determined this by comparing Figs. 5, 6, and 8. The elevation variation in the center of the micropeened MSM element was strikingly similar to that of the polished MSM element, suggesting the mechanism must be very similar. In Fig. 14(b), we show a diagram of a packet of $V_{lamellar}$ moving from left to right through the parent lamellar. The slight difference in the transition position of (5) suggests slight differences in the packet width. The CW twin packet was wide, similar to that for the thick twin packet in the polished sample. The CCW twin packet was a thinner band. This observation provides the basis of the difference between the actuation envelopes of the CW and CCW rotation directions. The CW rotation has a wide twin packet, resulting in greater actuation, while the CCW rotation has a thinner twin packet and deforms less.

5.4 Magnetic interaction with the twin structures.

Magnetic flux creates the magnetostress, which causes twin boundary motion. The driving magnetic field is created by the same mechanism: the rotating diametrically magnetized permanent magnet. The flux pattern, however, depends upon the interaction of the magnetic field with the twin microstructure due to the high magnetic anisotropy and the misorientation between the two domains. We modeled the difference between the flux pattern for the coarse twin microstructure and the lamellar microstructure.

We find the flux pattern is similar for both twin microstructures. Twin boundaries within the element refract the magnetic lines according to their volume fraction of each domain [39-41]. Thus, a $V_{lamellar}$ packet, which is near full strain (almost entirely blue according to Fig. 14), refracts flux approximately similar to a thick V_{twin}, as seen by comparing Figs. 10a and 10b. However, the magnetic flux refraction is less and smoother, as the $V_{lamellar}$ packet cannot fully be transformed to the blue domain, Fig. 14b.

5.5 Application of localized actuation to an MSM device: the MSM micropump

The MSM micropump is a simple extension of this actuation mechanism. We put a plate on top of the MSM element, with inlet and outlet holes centered at ±3 mm from the element center. Rotation of the permanent magnet causes a trough to form under the inlet, then to translate to the outlet, and finally to dissolve under the outlet. If the inlet contains fluid, the formation of the trough captures the fluid, translation of the trough transports the fluid, and dissolution of the trough ejects the fluid into the outlet. As shown by Chmielus *et al.* [19], coarse twins are stochastic, snapping from one stable position to the next, which causes the material to flow in a serrated fashion. The rapid, stochastic snapping of the material causes unsteady fluid flow in micropumps, resulting in a serrated output flow rate, seen for example in Saren *et al.* [26] and is responsible for shorter fatigue life [42].

A smooth, controlled trough is advantageous to the performance of the MSM pump. Smooth, controlled actuation gives flow stability and repeatability. Repeatable behavior allows for better sealing. The addition of the crest prevents backflow and results in higher head pressure. The oriented dense-twin microstructure and compressive surface stress layer yield a good fatigue life for the pump element [18].

The flowrate reported for the MSM micropump has a strong resemblance to the elevation variation measured at the center of the MSM element (Fig. 6). In Fig. 15, we plot the flowrate as a function of field angle for a similarly sized MSM micropump made from a micropeened element [43]. In this figure, data for fifty magnet revolutions are overlaid.

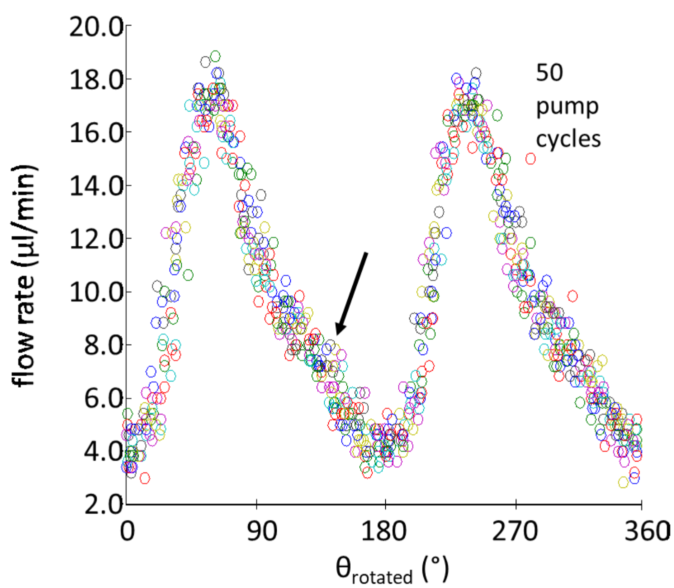

Fig. 15: Fifty MSM micropump cycles were superimposed, detailed, and adapted with permission from [43]. $\theta_{rotated}$ refers to elapsed angle, and is a temporal unit not based upon field orientation, unlike α in this study, which is a spatial coordinate of magnet field angle. Used as a micropump, the flowrate shows a similar modulation to that of the central elevation variation of the element in Fig. 6. The black arrow shows a transition point also marked in Fig. 6 as (5). We interpret the point as being the transition between $V_{lamellar}$ thickening and $V_{lamellar}$ motion down the element.

The flowrate has nearly identical features to the temporal elevation variation, including even the shoulder marked by the arrow. At the element center, the MSM element experiences the maximum trough depth (Fig. 5c, 5d). The results indicate that this depth determines the MSM pump flowrate per cycle.

The induced magnetic field pattern inside the element depends strongly on the orientation of the magnetic field relative to the twin boundaries. The highest flux condition occurs when the flux can enter the V_{twin} domain vertically, then be directed orthogonally by the twin boundary into H_{twin}. Such condition occurs early during the CW rotation and nucleates a large trough/crest couple. During the CCW rotation, the condition occurs after the pump cycle, and therefore after trough/crest nucleation.

The crests on either side of the trough in the micropeened sample (Fig. 5c, $\alpha = 18°$) have ramifications to the MSM micropump performance. Whereas a trough acts as a "negative displacement" mechanism and draws fluid in by creating a vacuum, the crest acts more akin to the traditional peristaltic motion of larger pumps, which drives the fluid forward. Knowing the geometry of the trough in each "step" of a cycle is important to understanding the behavior seen in MSM micropumps. The asymmetry of the surface profiles clearly explains the asymmetry seen between forward and reverse flow found in MSM micropumps [25, 26].

6. Summary and Conclusion:

We compared profilometry and optical experiments to model the actuation behavior of the Ni-Mn-Ga element and to understand the corresponding flowrate obtained with a pump made from a similar MSM element. We studied the effects of two different surface treatments on a single MSM element: polishing and micropeening. The polished element had a sharp-featured, faceted trough shape. The micropeened element had a smooth trough shape, forming an additional crest at the shoulders of the trough. Both microstructures have the same macroscopic motion: a twin packet that nucleates and moves through the element. The motion mechanism differed on the microscale. The packet is a single V_{twin} in the case of the polished sample, and it is a lamellar with a large twin volume fraction in the case of the micropeened element. The $V_{lamellar}$ approximates the single thick V_{twin} while allowing for both crests and troughs since the initial domain volume has differing fractions of the parent and twin. The dense twin microstructure smoothed the magnetic flux lines, thereby smoothening the element's behavior. Understanding these surface undulations, which give the actuator behavior, is a prerequisite to building high pressure, high repeatability MSM micropumps.

Acknowledgment

We acknowledge Brent Johnston for his contributions in designing and building the laser measurement stage and the microscopy test block. We recognize Paul Lindquist for contributing to the conceptual design of the laser measurement system. This research was funded by NSF STTR Phase I Grant 1622856 and NSF DMR 1710640.

References

[1] F. Li, S.J. Zhang, Z. Xu, X.Y. Wei, J. Luo, T.R. Shrout, Composition and phase dependence of the intrinsic and extrinsic piezoelectric activity of domain engineered (1-x)Pb(Mg1/3Nb2/3)O-3-xPbTiO(3) crystals, Journal of Applied Physics 108(3) (2010).
[2] Y. Ting, L.C. Chen, C.C. Li, J.L. Huang, Traveling-wave piezoelectric linear motor part I: The stator design, Ieee Transactions on Ultrasonics Ferroelectrics and Frequency Control 54(4) (2007) 847-853.
[3] K. Ullakko, L. Wendell, A. Smith, P. Müllner, G. Hampikian, A magnetic shape memory micropump: contact-free, and compatible with PCR and human DNA profiling, Smart Materials and Structures 21(11) (2012).
[4] K. Ullakko, J.K. Huang, C. Kantner, R.C. Ohandley, V.V. Kokorin, Large magnetic-field-induced strains in Ni2MnGa single crystals, Applied Physics Letters 69(13) (1996) 1966-1968.
[5] V. Chernenko, E. Cesari, V. Kokorin, I. Vitenko, The development of new ferromagnetic shape memory alloys in Ni-Mn-Ga system, Scripta metallurgica et materialia 33(8) (1995) 1239-1244.
[6] V.V. Kokorin, V.A. Chernenko, V.I. Valkov, S.M. Konoplyuk, E.A. Khapalyuk, Magnetic transformation in Ni2MnGa compounds, Fizika Tverdogo Tela 37(12) (1995) 3718-3722.
[7] S.J. Murray, M.A. Marioni, A.M. Kukla, J. Robinson, R.C. O'Handley, S.M. Allen, Large field induced strain in single crystalline Ni-Mn-Ga ferromagnetic shape memory alloy, Journal of Applied Physics 87(9) (2000) 5774-5776.
[8] A. Sozinov, D. Musiienko, A. Saren, P. Vertat, L. Straka, O. Heczko, M. Zeleny, R. Chulist, K. Ullakko, Highly mobile twin boundaries in seven-layer modulated Ni-Mn-Ga-Fe martensite, Scripta Materialia 178 (2020) 62-66.
[9] N.J. Kucza, C.L. Patrick, D.C. Dunand, P. Müllner, Magnetic-field-induced bending and straining of Ni–Mn–Ga single crystal beams with high aspect ratios, Acta Materialia 95 (2015) 284-290.
[10] R. Chulist, L. Straka, H. Seiner, A. Sozinov, N. Schell, T. Tokarski, Branching of {110) twin boundaries in five-layered Ni-Mn-Ga bent single crystals, Materials & Design 171 (2019).
[11] L. Straka, N. Lanska, K. Ullakko, A. Sozinov, Twin microstructure dependent mechanical response in Ni-Mn-Ga single crystals, Applied Physics Letters 96(13) (2010).
[12] A. Smith, J. Tellinen, P. Müllner, K. Ullakko, Controlling twin variant configuration in a constrained Ni-Mn-Ga sample using local magnetic fields, Scripta Materialia 77 (2014) 68-70.
[13] O. Heczko, Magnetic shape memory effect and highly mobile twin boundaries, Materials Science and Technology 30(13A) (2014) 1559-1578.
[14] E. Pagounis, R. Chulist, M. Szczerba, M. Laufenberg, High-temperature magnetic shape memory actuation in a Ni–Mn–Ga single crystal, Scripta Materialia 83 (2014) 29-32.
[15] L. Straka, O. Heczko, Magnetic anisotropy in Ni–Mn–Ga martensites, Journal of Applied Physics 93(10) (2003) 8636-8638.
[16] L. Straka, A. Soroka, H. Seiner, H. Hanninen, A. Sozinov, Temperature dependence of twinning stress of Type I and Type II twins in 10M modulated Ni-Mn-Ga martensite, Scripta Materialia 67(1) (2012) 25-28.
[17] D. Kellis, A. Smith, K. Ullakko, P. Müllner, Oriented single crystals of Ni-Mn-Ga with very low switching field, Journal of Crystal Growth 359 (2012) 64-68.
[18] H. Zhang, A. Armstrong, P. Müllner, Effects of surface modifications on the fatigue life of unconstrained Ni-Mn-Ga single crystals in a rotating magnetic field, Acta Materialia 155 (2018) 175-186.

[19] M. Chmielus, C. Witherspoon, K. Ullakko, P. Müllner, R. Schneider, Effects of surface damage on twinning stress and the stability of twin microstructures of magnetic shape memory alloys, Acta Materialia 59(8) (2011) 2948-2956.
[20] A. Tech, Y. Ezer, A. Soroka, L. Straka, Method of producing magnetic shape memory alloy elements and the use thereof, Adaptamat, USA, 2012.
[21] M. Chmielus, K. Rolfs, R. Wimpory, W. Reimers, P. Müllner, R. Schneider, Effects of surface roughness and training on the twinning stress of Ni-Mn-Ga single crystals, Acta Materialia 58(11) (2010) 3952-3962.
[22] D. Musiienko, A.R. Smith, A. Saren, K. Ullakko, Stabilization of a fine twin structure in Ni-Mn-Ga by a diamond-like carbon coating, Scripta Materialia 106 (2015) 9-12.
[23] K. Ullakko, M. Chmielus, P. Müllner, Stabilizing a fine twin structure in Ni-Mn-Ga samples by coatings and ion implantation, Scripta Materialia 94 (2015) 40-43.
[24] L. Straka, H. Hänninen, A. Soroka, Y. Ezer, Enhanced Fatigue Behavior of Ni-Mn-Ga Magnetic Shape Memory Alloys with Tailor-made Fine Twin Microstructure, 13th International Conference on New Actuators, Bremen, Germany, 2012.
[25] A.R. Smith, A. Saren, J. Jarvinen, K. Ullakko, Characterization of a high-resolution solid-state micropump that can be integrated into microfluidic systems, Microfluidics and Nanofluidics 18(5-6) (2015) 1255-1263.
[26] A. Saren, A.R. Smith, K. Ullakko, Integratable magnetic shape memory micropump for high-pressure, precision microfluidic applications, Microfluidics and Nanofluidics 22(4) (2018).
[27] S. Barker, E. Rhoads, P. Lindquist, M. Vreugdenhil, P. Müllner, Magnetic Shape Memory Micropump for Submicroliter Intracranial Drug Delivery in Rats, Journal of Medical Devices-Transactions of the Asme 10(4) (2016).
[28] L. Straka, O. Heczko, Superelastic response of Ni-Mn-Ga martensite in magnetic fields and a simple model, Ieee Transactions on Magnetics 39(5) (2003) 3402-3404.
[29] H.P. Feigenbaum, C. Ciocanel, J.L. Eberle, J.L. Dikes, Experimental characterization and modeling of a three-variant magnetic shape memory alloy, Smart Materials and Structures 25(10) (2016) 16.
[30] B. Kiefer, H.E. Karaca, D.C. Lagoudas, I. Karaman, Characterization and modeling of the magnetic field-induced strain and work output in Ni2MnGa magnetic shape memory alloys, Journal of Magnetism and Magnetic Materials 312(1) (2007) 164-175.
[31] P.J. Brown, J. Crangle, T. Kanomata, M. Matsmuoto, K.U. Neumann, B. Ouladdiaf, K.R.A. Ziebeck, The crystal structure and phase transitions of the magnetic shape memory compound Ni2MnGa, Journal of Physics-Condensed Matter 14(43) (2002) 10159-10171.
[32] J. Pons, V.A. Chernenko, R. Santamarta, E. Cesari, Crystal structure of martensitic phases in Ni-Mn-Ga shape memory alloys, Acta Materialia 48(12) (2000) 3027-3038.
[33] I. Suorsa, E. Pagounis, K. Ullakko, Position dependent inductance based on magnetic shape memory materials, Sensors and Actuators a-Physical 121(1) (2005) 136-141.
[34] M. Chmielus, I. Glavatskyy, J.U. Hoffmann, V.A. Chernenko, R. Schneider, P. Müllner, Influence of constraints and twinning stress on magnetic field-induced strain of magnetic shape-memory alloys, Scripta Materialia 64(9) (2011) 888-891.
[35] H.D. Chopra, C. Bailly, M. Wuttig, Domain structures in bent In-22.5 at.%Tl polydomain crystals, Acta Materialia 44(2) (1996) 747-751.
[36] M. Chmielus, P. Müllner, Effects of Surface Pinning, Locking and Adaption of Twins on the Performance of Magnetic Shape-Memory Alloys, Trans Tech Publ, pp. 177-201.
[37] P. Müllner, G. Kostorz, Microstructure of Magnetic Shape-Memory Alloys: Between Magnetoelasticity and Magnetoplasticity, Materials Science Forum 583 (2008) 43-65.
[38] O. Heczko, L. Straka, H. Seiner, Different microstructures of mobile twin boundaries in 10 M modulated Ni-Mn-Ga martensite, Acta Materialia 61(2) (2013) 622-631.

[39] B. Krevet, M. Kohl, P. Morrison, S. Seelecke, Magnetization- and strain-dependent free energy model for FEM simulation of magnetic shape memory alloys, European Physical Journal-Special Topics 158 (2008) 205-211.
[40] T. Schiepp, M. Maier, E. Pagounis, A. Schluter, M. Laufenberg, FEM-Simulation of Magnetic Shape Memory Actuators, Ieee Transactions on Magnetics 50(2) (2014).
[41] K. Haldar, B. Kiefer, D.C. Lagoudas, Finite element analysis of the demagnetization effect and stress inhomogeneities in magnetic shape memory alloy samples, Philosophical Magazine 91(32) (2011) 4126-4157.
[42] O. Soderberg, Y. Ge, A. Sozinov, S.P. Hannula, V.K. Lindroos, Recent breakthrough development of the magnetic shape memory effect in Ni-Mn-Ga alloys, Smart Materials and Structures 14(5) (2005) S223-S235.
[43] *A. Armstrong* , B. Johnston, P. Lindquist, A. Smith, P. Müllner, Analysis of individual cycle deformation in Ni-Mn-Ga micropumps, Proceedings of the international conference ACTUATOR'18, Bremen, Germany, 2018, pp. 235-238.